

The obliquity and atmosphere of the hot Jupiter WASP-122b (KELT-14b) with ESPRESSO: An aligned orbit and no sign of atomic or molecular absorption*

M. Stangret¹, E. Pallé^{2,3}, E. Esparza-Borges^{2,3}, J. Orell Miquel^{2,3}, N. Casasayas-Barris², M. R. Zapatero Osorio⁴, E. Cristo^{5,6}, R. Allart^{7,8}, Y. Alibert⁹, F. Borsa¹⁰, O. D. S. Demangeon^{5,6}, P. Di Marcantonio¹¹, D. Ehrenreich^{8,12}, P. Figueira^{8,5}, J. I. González Hernández^{2,3}, E. Herrero-Cisneros¹⁶, C. J. A. P. Martins^{13,5}, N. C. Santos^{5,6}, J. V. Seidel¹⁴, T. Azevedo Silva^{5,6,17}, A. Sozzetti¹⁵, M. Steiner⁸, A. Suárez Mascareño^{2,3}, and S. Udry⁸

¹ INAF – Osservatorio Astronomico di Padova, Vicolo dell’Osservatorio 5, 35122, Padova, Italy
e-mail: monika.beata.stangret@gmail.com

² Instituto de Astrofísica de Canarias (IAC), 38205 La Laguna, Tenerife, Spain

³ Departamento de Astrofísica, Universidad de La Laguna (ULL), 38206, La Laguna, Tenerife, Spain

⁴ Centro de Astrobiología, CSIC-INTA, Camino Bajo del Castillo s/n, 28692, Villanueva de la Cañada, Madrid, Spain

⁵ Instituto de Astrofísica e Ciências do Espaço, CAUP, Rua das Estrelas, 4150-762 Porto, Portugal

⁶ Departamento de Física e Astronomia, Faculdade de Ciências, Universidade do Porto, Rua Campo Alegre, 4169-007 Porto, Portugal

⁷ Département de Physique, Institut Trotter de Recherche sur les Exoplanètes, Université de Montréal, Montréal, Québec, H3T 1J4, Canada

⁸ Observatoire Astronomique de l’Université de Genève, Chemin Pegasi 51, Sauverny, CH-1290, Switzerland

⁹ Physics Institute of University of Bern, Gesellschafts strasse 6, 3012, Bern, Switzerland

¹⁰ INAF – Osservatorio Astronomico di Brera, Via Bianchi 46, 23807 Merate, Italy

¹¹ INAF – Osservatorio Astronomico di Trieste, via G. B. Tiepolo 11, I-34143, Trieste, Italy

¹² Centre Vie dans l’Univers, Faculté des sciences de l’Université de Genève, Quai Ernest-Ansermet 30, 1205 Geneva, Switzerland

¹³ Centro de Astrofísica da Universidade do Porto, Rua das Estrelas, 4150-762 Porto, Portugal

¹⁴ European Southern Observatory (ESO), Alonso de Córdova 3107, Vitacura, Casilla 19001, Santiago de Chile, Chile

¹⁵ INAF – Osservatorio Astrofisico di Torino, Via Osservatorio 20, 10025 Pino Torinese, Italy

¹⁶ Centro de Astrobiología, CSIC-INTA, Crta. Ajalvir km 4, E-28850 Torrejón de Ardoz, Madrid, Spain

¹⁷ INAF - Osservatorio Astrofisico di Arcetri, Largo Enrico Fermi 5, I-50125 Firenze, Italy

ABSTRACT

Thanks to their short orbital periods and hot extended atmospheres, hot Jupiters are ideal candidates for atmosphere studies with high-resolution spectroscopy. New stable spectrographs help improve our understanding of the evolution and composition of those types of planets. By analyzing two nights of observations using the ESPRESSO high-resolution spectrograph, we studied the architecture and atmosphere of hot Jupiter WASP-122b (KELT-14b). By analyzing the Rossiter-McLaughlin (RM) effect, we measured the spin-orbit angle of the system to be $\lambda = 0.09^{+0.88}_{-0.90}$ deg. This result is in line with literature obliquity measurements of planetary systems around stars with effective temperatures cooler than 6500 K. Using the transmission spectroscopy, we studied the atmosphere of the planet. Applying both the single-line analysis and the cross-correlation method, we looked for Ca I, Cr I, Fe I, Fe II, H₂O, Li I, Mg I, Na I, Ti I, TiO, V I, VO, and Y I. Our results show no evidence of any of these species in WASP-122b’s atmosphere. The lack of significant detections can be explained by either the RM effect covering the regions where the atmospheric signal is expected and masking it, along with the low signal-to-noise ratio (S/N) of the observations or the absence of the relevant species in its atmosphere.

Key words. planetary systems – planets and satellites: individual: WASP-122b, KELT-14b – planets and satellites: atmospheres – methods: observational – techniques: spectroscopic

1. Introduction

High-resolution spectroscopic observations are powerful tools for characterizing exoplanetary atmospheres. Thanks to different radial velocities, we are able to differentiate the signal coming from the Earth’s atmosphere, the host star, and the atmosphere of the exoplanet. Hot Jupiters (HJ, $T_{\text{eq}} < 2000$ K) and

ultra-hot Jupiters (UJ, $T_{\text{eq}} > 2000$ K), namely, gas giant planets with short orbital periods that are close to their host stars with hot and extended atmospheres, are the most suitable exoplanets for these studies. It is believed that due to their tidally locked nature leading to a large temperature gradient within the atmosphere, the chemistry in the night and day regions of the planet can be different (Arcangeli et al. 2018).

Recent transmission spectroscopic studies of the atmospheres of hot Jupiters using ground-based telescopes show a variety of species in their atmospheres. The most comprehensive

* Based on Guaranteed Time Observations collected at the European Southern Observatory under ESO program 106.21M2.004 by the ESPRESSO Consortium.

studies of HJ using high-resolution transmission spectroscopic observations have been performed on HD 189733b (Salz et al. 2018; Alonso-Floriano et al. 2019a; Cabot et al. 2019; Brogi & Line 2019; Guilluy et al. 2020; Boucher et al. 2021; Cristo et al. 2022, 2024) and HD 209458b (Snellen et al. 2010; Brogi & Line 2019; Alonso-Floriano et al. 2019b; Sánchez-López et al. 2019; Santos et al. 2020; Giacobbe et al. 2021; Casasayas-Barris et al. 2021). The planets show the presence of molecules like H₂O, CO, HCN, CH₄, and NH₃, along with He I and Na I.

High-resolution detections of atoms and molecules were presented in several other HJs: 51 Pegb (Birkby et al. 2017; Chiavassa & Brogi 2019), HD 102195b (Guilluy et al. 2019), HD 149026b (Ishizuka et al. 2021), tau Boo Ab (Brogi et al. 2012; Lockwood et al. 2014; Webb et al. 2022), WASP-21b (Chen et al. 2020a), WASP-52b (Chen et al. 2020b), WASP-69b (Nortmann et al. 2018; Casasayas-Barris et al. 2017; Khalafinejad et al. 2021), WASP-77Ab (Line et al. 2021), WASP-127b (Allart et al. 2020; Boucher et al. 2023; Nortmann et al. 2024), and WASP-172b (Seidel et al. 2023). The list of detected species consists of C I, CO, Fe I, H I, H₂O, He I, K I, Na I, OH, and Ti I.

Compared to hot Jupiters, due to the much higher equilibrium temperatures, in ultra-hot Jupiters we expect mostly neutral and ionized atoms, where most of the molecules are dissociated. For example, KELT-9b, the hottest UHJ known to date, shows the presence of Ca I, Ca II, Cr I, Cr II, Fe I, Fe II, H, Mg II, the Mg triplet, Ni I, O I, Na I, Sc II, Sr II, Tb II, Ti II, Y II, and evidence of Co I and Sr II (Yan & Henning 2018; Hoeijmakers et al. 2018; Cauley et al. 2019; Hoeijmakers et al. 2019; Yan et al. 2019; Pino et al. 2020; Wyttenbach et al. 2020; Borsa et al. 2021).

In addition to the atmospheric composition, precise radial velocity measurements and analysis of the spectral line deformation, the so-called Rossiter-McLaughlin effect (Holt 1893; Schlesinger 1910; Rossiter 1924; McLaughlin 1924) allows us to measure the sky-projected spin-orbit angle (λ). This allows us to gain valuable insight into the architecture of the system and to differentiate between different models of planetary migration (cite). It has been observed that planets orbiting stars with the $T_{eff} < 6250$ K (Winn 2010) are located on aligned orbits, while the planets orbiting warmer stars to do follow this trend. This behavior is explained by the Kraft break (Kraft 1967), where the stars with $T_{eff} < 6250$ K experience angular momentum loss, which affects the spin-orbit alignment. The measurements of the obliquity of the system were successfully obtained for ~ 200 transiting exoplanets (i.e., Winn et al. 2006; Esposito et al. 2017; Addison et al. 2018; Oshagh et al. 2018; Wang et al. 2018; Casasayas-Barris et al. 2020; Palle et al. 2020; Bourrier et al. 2021; Stangret et al. 2021).

These studies are possible thanks to the new generation of high-resolution spectrographs such as Echelle Spectrograph for Rocky Exoplanets and Stable Spectroscopic Observations (ESPRESSO, Pepe et al. 2021). ESPRESSO is a fiber-fed échelle high-resolution spectrograph ($\mathcal{R} \sim 140,000$) mounted on the Very Large Telescope (VLT), in Cerro Paranal, Chile. The spectrograph covers the wavelength from 380 to 788 nm. It can be used on any of the four Unit Telescopes (UTs), as well as on four UTs simultaneously.

In this work, we present studies of the architecture and atmosphere of hot Jupiter WASP-122b (Turner et al. 2016) also known as KELT-14b (Rodríguez et al. 2016), using the ESPRESSO spectrograph in single UT mode (singleHR21-high-resolution mode with 2x1 binning). The planet orbits a G2 star near the main sequence turnoff ($T_{eff} = 5802$ K, $M_{\star} = 1.178 M_{\odot}$, $R_{\star} = 1.368 R_{\odot}$) with a period of 1.71 days. WASP-122b is an inflated gas giant planet with a mass of 1.196 M_J and a radius

of 1.52 R_J. Due to its close distance to the host star, WASP-122b has a high equilibrium temperature of 1904 ± 54 K. Its temperature, as well as the brightness of the star ($V = 11$ mag), make this planet suitable for studying the chemical properties of its atmosphere using high-resolution ground-based spectrographs. All parameters of the star, the planet, and the system can be found in Table 1. In Fig. 1, we present the context of WASP-122b with respect to all known planets with $T_{eq} > 1400$ K and $R_p > 0.6 R_J$, depending on their equilibrium temperature versus surface gravity and transmission spectroscopy metrics (TSM, Kempton et al. 2018). A TSM of ~ 180 puts WASP-122b in the region where atmospheric chemistry is possible, but its study is not straightforward.

Table 1: Physical and orbital parameters of the WASP-122 system.

Parameter	Value
<i>..... Stellar parameters</i>	
T_{eff} [K]	5802^{+95}_{-92}
$\log g$ [cgs]	$4.234^{+0.045}_{-0.041}$
[Fe/H]	$0.326^{+0.091}_{-0.089}$
M_{\star} [M_{\odot}]	$1.178^{+0.052}_{-0.066}$
R_{\star} [R_{\odot}]	$1.368^{+0.078}_{-0.077}$
$v \sin i_{\star}^a$ [km s ⁻¹]	1.84 ± 0.08
<i>..... Planet parameters</i>	
M_p [M_J]	1.196 ± 0.072
R_p [R_J]	$1.52^{+0.12}_{-0.11}$
T_{eq} [K]	1904 ± 54
K_p^a [km s ⁻¹]	185 ± 4
<i>..... Transit parameters</i>	
T_0^b [BJD _{TDB}]	$2457872.52231 \pm 0.00015$
P^b [days]	$1.71005344 \pm 0.00000032$
T_{14}^c [days]	$0.0889^{+0.0025}_{-0.0026}$
<i>..... System parameters</i>	
a/R_{\star}	$4.64^{+0.25}_{-0.22}$
R_p/R_{\star}	$0.1143^{+0.0029}_{-0.0026}$
i_p [deg]	$79.67^{+0.80}_{-0.77}$
λ^a [deg]	$0.09^{+0.88}_{-0.90}$

Notes. The physical and orbital parameters for the WASP-122 system were adopted from Rodríguez et al. (2016), except for ^(a) value retrieved in this work and ^(b) adopted from Edwards et al. (2021). ^(c) T_{14} is the total transit duration, between the first and fourth contacts of the transit.

This paper is structured as follows. In Sect. 2, we describe the observations and data reduction, in Sect. 3 we describe the obliquity measurements. Sections 4 and 5 describe the transmission spectra analysis, focusing on single lines and using the cross-correlation method, respectively. The final results are discussed and concluded in Sect. 6.

2. Observations and data reduction

We observed two full transits of WASP-122b during the nights of 18 January 2021 and 12 February 2021 (hereafter referred to as Night 1 and Night 2), with the ESPRESSO spectrograph (Guaranteed Time Observation, program 106.21M2.004). During Night 1, we took 58 spectra with an exposure time of 300 s, 38 out-of-transit and 20 in-transit spectra, covering the planetary orbital phases $\phi = -0.073$ to $\phi = 0.073$ with a mean signal-to-noise ratio (S/N) of 34.9 around 590 nm (physical echelle order 104).

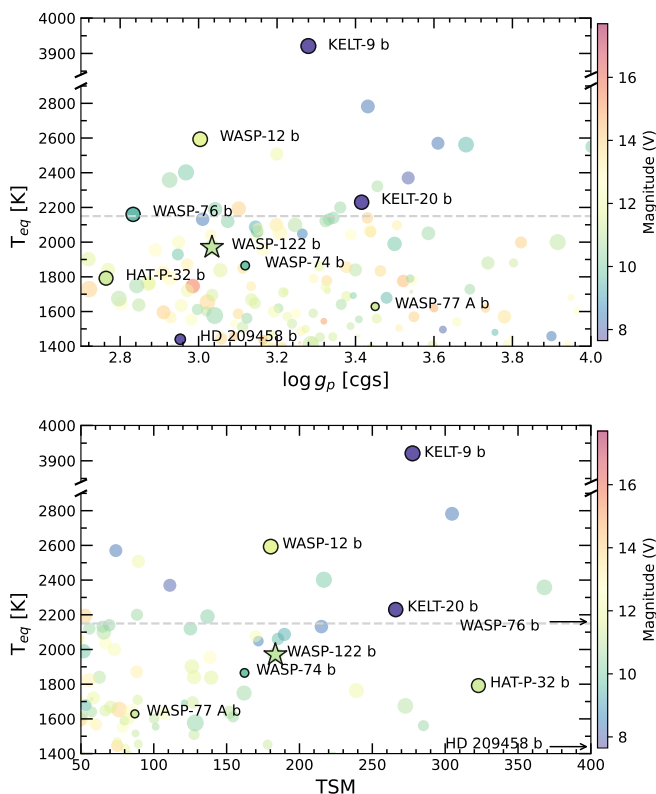


Fig. 1: Context of WASP-122b, marked with a star symbol, with respect to all known planets with $T_{eq} > 1400\text{K}$ and $R_p > 0.6 R_J$. The equilibrium temperature is plotted on the vertical axis and surface gravity (top panel), and the transmission spectroscopy metrics (bottom panel) are plotted on the horizontal axis. The gray horizontal line in the temperature where we differentiate the HJ and UHJ according to Stangret et al. (2022) at 2150 K. For both figures, the size of the marker indicates the planetary radius and the V-band magnitude of the host star is color-coded.

During Night 2, we took 48 spectra with an exposure time of 400 s, 31 out-of-transit and 17 in-transit spectra covering the planetary orbital phases $\phi = -0.072$ to $\phi = 0.074$ with mean S/N of 43.4 around 590 nm. Observing log can be found in Table 2. The data were reduced using the Data Reduction Software (DRS) pipeline 2.2.8 and s1d sky-subtracted spectra were used in this work. The S/N and airmass evolution plots for each of the nights are shown in Fig. 2.

3. Obliquity measurement

The classical Rossiter-McLaughlin (RM) effect offers information about the planet-star radius ratio, the rotational velocity of the host star, impact parameter, and obliquity of the system (Triaud 2018). In particular, the modeling of the RM effect has been widely used in the literature as a tool to measure the sky-projected spin-orbit angle λ (i.e., Addison et al. 2018; Oshagh et al. 2018; Wang et al. 2018; Casasayas-Barris et al. 2020; Palle et al. 2020; Bourrier et al. 2021).

Here, we analyzed the RM signal present in the radial velocity (RV) measurements extracted by the DRS pipeline from both ESPRESSO datasets using G8 binary mask. For each of the relevant nights, we extracted the RM signal by subtracting a linear fit to the out-of-transit RVs. Subsequently, we combined both

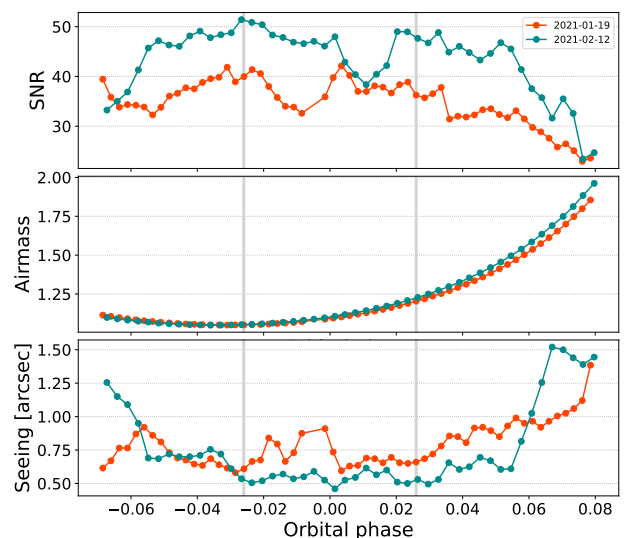


Fig. 2: S/N (top panel) in the Na I echelle order (order 104), airmass (middle panel), and seeing (calculated as the mean seeing at the beginning and end of the exposure) evolution during the two nights of observations. Gray vertical lines represent the beginning (T1) and end (T4) of the transit.

data sets by sorting them in orbital phase. In Fig. 3 we plot the measurements from each of the separate nights.

The approach used by the ESPRESSO DRS pipeline to measure the RVs is based on the fitting of a Gaussian to the cross-correlation function (CCF), which is a function obtained from the cross-correlation of a spectrum with a binary mask (this technique is detailed in Pepe et al. 2002). For this reason, to model the RM signal, we used a Python implementation of ARoME (Boué et al. 2013), which is a code specifically designed to model the RV data extracted by the CCF approach. We also utilized emcee (Foreman-Mackey et al. 2013) to perform a Markov chain Monte Carlo (MCMC) fitting procedure of the RM signal using the ARoME models. As free parameters, we took the mid-transit time (t_{mid}), the sky-projected spin-orbit angle (λ), and the projected stellar rotational velocity ($v \sin i$). We imposed large uniform priors on the free parameters: ($-0.02 \text{ days} < T_0 - t_{mid} < 0.02 \text{ days}$), ($-45 \text{ deg} < \lambda < 45 \text{ deg}$), and ($-30 \text{ km s}^{-1} < v \sin i < 30 \text{ km s}^{-1}$). Throughout the fitting, we fixed the rest of the planetary and stellar parameters, including the limb darkening coefficients, which were fixed to the values obtained through LDTk (Parviainen & Aigrain 2015) estimations. By assuming quadratic limb-darkening law the limb-darkening coefficients were fixed to $q_1 = 0.577 \pm 0.002$ and $q_2 = 0.113 \pm 0.003$.

As a result of the fitting procedure, we determined the sky-projected spin-orbit angle to be $\lambda = 0.09^{+0.88}_{-0.90}$ deg. In Fig. 3, we show the best RM model and the 1σ uncertainties from the fit, the fitted values are given in Table 3, and the corner plots from the fitting are shown in the A.9.

Thus, we found WASP-122b to be an aligned planet. In the top panel of Fig. 4, we compare WASP-122b to the rest of the known planets with an obliquity measurement in the $T_{eff} - \lambda$ plane, indicating the size of each planet in color. WASP-122b follows the general alignment trend shown by planets orbiting stars with effective temperatures cooler than 6250 K, and is one of the largest planets in this population. This T_{eff} is directly related to the Kraft Break (cite). Stars with $T_{eff} < 6250 \text{ K}$ experience angular momentum loss due to a large convective

Table 2: Observing log of WASP-122b transit observations.

Night	Date of observation	Telescope	Start [UT]	End [UT]	Airmass ^(a) change	T_{exp} [s]	N_{obs}	S/N ^(b)
1	2021-01-19	VLT-UT2	02:27	08:30	1.11-1.12-1.86	300	58	22.9-41.1
2	2021-02-12	VLT-UT3	01:04	07:06	1.10-1.13-1.96	400	48	23.4-51.4

Notes. ^(a) Airmass change during the observations, where the values represent, airmass at the beginning of the nights, mid-observations, and at the end of the night, respectively. ^(b) Minimum and maximum S/N for each night, calculated in Na I echelle order (physical order 104).

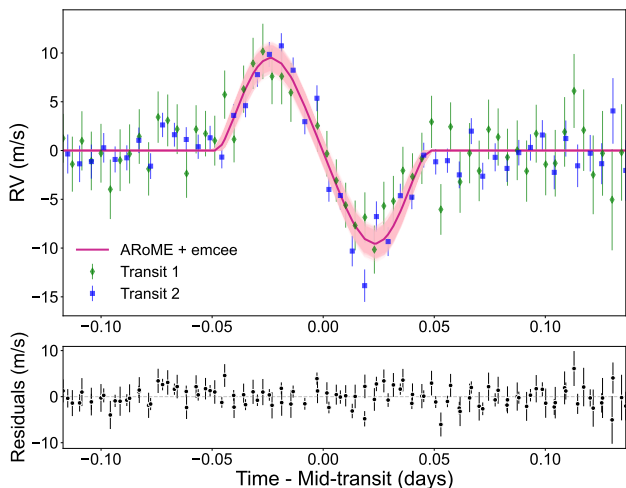


Fig. 3: The Rossiter-McLaughlin signal from the Night 1 (green diamonds) and Night 2 (blue squares) RV time series (top). The solid lines show the best RM model resulting from the ARoME + emcee fitting (magenta) and models within 1σ (light pink). Bottom panel shows the residuals.

zone, which directly influences the spin-orbit angle of the planets around them.

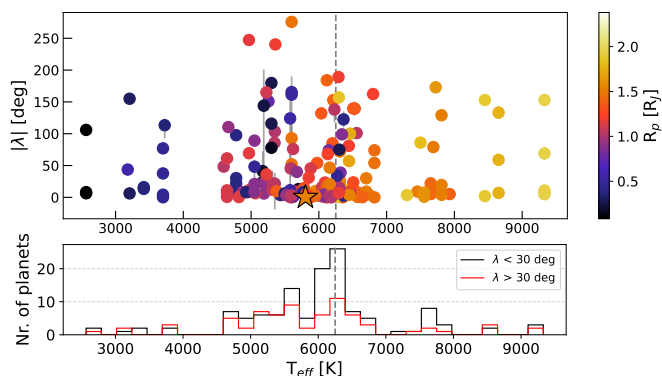


Fig. 4: WASP-122b in the $T_{\text{eff}} - |\lambda|$ plane compared to the rest of the confirmed planets with an obliquity measurement (top). The colors indicate the planetary radius. WASP-122b is marked with a "star" symbol. The sample of planets with an obliquity measurement was extracted from the TEPcat catalog (Southworth 2011). In the case of planets with more than one measurement, we plot the mean of those values, with the error bar indicating the span between the maximum and minimum literature values. Bottom panel: Histogram of number of planets with $\lambda > 30$ deg and $\lambda < 30$ deg, depending on the T_{eff} of their main star. In both panels, vertical grey dashed lines indicate the $T_{\text{eff}} = 6250$ K.

Table 3: Emcee + PyArome combined fitting results of the parameters.

Parameter	Value
$T_0 - t_{\text{mid}}$ [days]	0.0002 ± 0.0007
λ [deg]	$0.09^{+0.88}_{-0.90}$
$v \sin i$ [km s ⁻¹]	1.84 ± 0.08

There is no rotation period available for the star WASP-122b in the literature, since the star is inactive Turner et al. 2016. Thus, measuring the starspot rotational period using spectroscopic time series is extremely difficult, so the true obliquity angle of the planetary system cannot be determined. However, if the system is synchronized (expected given the mass and short orbital period of the planet, Rodriguez et al. 2016) and both star and planet share the same rotation rate, we can estimate an obliquity angle of $\psi = \pm 77.06 \pm 0.86$ deg.

4. Transmission spectroscopy around single lines

Following the methodology presented in Wyttenbach et al. (2015) and Casasayas-Barris et al. (2018), and later applied to ESPRESSO data in Casasayas-Barris et al. (2021), we determined the transmission spectrum of WASP-122b around several atmospheric lines previously found in hot atmospheres; namely: the Na I doublet ($\lambda 5891\text{\AA}$ and $\lambda 5897\text{\AA}$), H α , H β , and Li I ($\lambda 6709\text{\AA}$).

The extracted spectra were first telluric corrected using the Molecfit code (Smette et al. 2015, Kausch et al. 2015), and then shifted to the stellar rest frame, taking into account the barycentric correction, the systemic velocity, and the movements of the star around the center of mass of the system; the latter were corrected by fitting the linear function to all of the out-of-transit radial velocity measurements, assuming eccentricity equal to zero (Turner et al. 2016, Rodriguez et al. 2016). After normalizing the spectrum, the stellar signal was removed by dividing each spectrum by the master-out spectrum, calculated as the mean of all of the out-of-transit spectra. The resulting residuals were then shifted to the planetary rest frame using the formula:

$$v_p(t, K_p) = K_p \sin 2\pi\phi(t), \quad (1)$$

where v_p is the radial velocity of the planet, K_p is the semi-amplitude of the exoplanet radial velocity, and ϕ is the orbital phase of the planet. In this case, we assumed the K_p to be 185 km s^{-1} , which is equal to the predicted K_p value calculated using the orbital parameters from Table 1. Finally, all in-transit residuals were combined to obtain the exoplanet's transmission spectrum. As shown in several previous works using the ESPRESSO spectrograph (e.g., Allart et al. 2020, Tabernero et al. 2021,

Casasayas-Barris et al. 2021), the spectra are affected by two sinusoidal patterns created by the coude train optics, called “wiggles,” with periods of 30 Å and 1 Å. Due to the low S/N of the observations, the 1 Å wiggles were not detected. The wiggles with period 30 Å were not clearly detected in the single spectra in the regions around the studied lines, but created the sinusoidal structure in the final transmission spectrum. We corrected this anomaly locally around the studied line by fitting a fourth-order polynomial function.

After exploring the different spectral lines, we found no evidence of planetary absorption in any of them. In Fig. 5 we show the final results in the spectral region containing the Na I doublet. The top two panels show two-dimensional maps of the individual transmission spectra around the Na I doublet in the stellar and planetary rest frame, respectively. In the middle panels, we present similar maps as those in the top panels, but we have masked the regions ± 0.2 Å from the center of the lines affected by the residuals of the stellar Na I doublet. Calculations were repeated by masking the regions around the studied lines from ± 0.1 to ± 0.5 Å with similar results. The final transmission spectrum is shown in the bottom panel, without (red) and with (black) masking the stellar signals. The presented transmission spectrum shows no statistically significant features. Very similar results are found for the rest of the studied lines shown in Fig. A.1 for H α , Fig. A.2 for H β , and A.3 for Li I.

5. Survey of atomic and molecular species using the cross-correlation technique

To study the chemical atmospheric composition of WASP-122b, we applied the cross-correlation (CC) method to the data using a range of atoms and molecules: Ca I, Cr I, FeH, Fe I, Fe II, H₂O, K I, Mg I, Na I, Ti I, TiO, V I, VO, and Y I. All the models were calculated with the petitRADTRANS code (Mollière et al. 2019) assuming solar abundances from Asplund et al. (2009), equilibrium chemistry, and two different temperatures $T_{eq} = 1904$ K (T_{eq} of the planet) and 4000 K. We tested models for two temperatures because observed regions can have much higher temperatures than T_{eq} . It is possible that spectral lines for the models created for lower temperatures may not exist, which would result in the species not being detected using the CC method. Due to the absence or weakness of spectral lines for Fe II and Mg I for $T_{eq} = 1904$ K, we decided not to show the results for these cases. In the case of TiO, we created two different models using the line lists provided by Exomol (McKemmish et al. 2019) and Plez (Plez 1998), both available in the petitRADTRANS code. Finally, the models were convolved to the resolution of the ESPRESSO spectrograph ($\mathfrak{R} = 140,000$). We did not convolve the models to the rotational period of the exoplanet or the exposure time because the difference in cross-correlation is insignificant and does not affect the final detection or non-detections. The models and information about the line list can be found in Fig. A.4.

We reduced the data following Stangret et al. (2022). In the first steps, we repeated the procedures from the analysis of the single lines, where the telluric lines were corrected with the Molecfit code, and the spectra were moved to the stellar rest frame. In the next step, we divided each spectrum into 10000-pixel orders, at each wavelength, excluding the pixels that were divided from fitted quadratic polynomials more than 5σ , which were related to the remaining hot and cold pixels. Each of the orders was normalized by fitting a quadratic polynomial. The emission lines larger than 5% were masked. Finally, the stellar

signal was removed by dividing each spectrum by the master-out spectrum, calculated as the mean of all of the out-of-transit spectra. Before the CC, we combined each order into one spectrum, masking the wavelengths < 4500 Å, where the S/N was low, and the regions between 6850-6950 Å and 7550-7700 Å, which are strongly affected by telluric lines.

Afterward, the residuals were cross-correlated with atmospheric models for radial velocities in the range of ± 300 km s⁻¹ with a step of 0.5 km s⁻¹, which corresponds to the pixel size of ESPRESSO. We removed a fourth-order polynomial from each of the CC residuals in time, which brought the CC values to a similar level. This procedure effectively removed the broadband structures, such as big wiggles, without affecting the possible detection of the sinusoidal signal, which is much wider (> 200 km s⁻¹) than the expected planetary signal. The residual maps for each of the species are presented in the left column of Fig. 7 and Fig. 8 for 1904 K and in Fig. A.5 and A.6 for 4000 K. In the next step, we shifted the maps to the planetary rest frame using Formula 1. In the case of the cross-correlation method, we assumed that K_p is unknown and calculated v_p for a range of K_p values from 0 to 300 km s⁻¹, in steps of 1 km s⁻¹. Afterward, in order to retrieve higher S/N, we co-added the in-transit (including ingress and egress) cross-correlation residuals. In the final step, we calculate the significance of the results by calculating the S/N by dividing the CC values by the standard deviation calculated around -150 km s⁻¹ to -50 km s⁻¹ and 50 km s⁻¹ to 150 km s⁻¹.

5.1. Rossiter-McLaughlin effect modelling and correction

Although WASP-122 is not a fast-rotating star, due to the high quality of the data we were able to detect the Rossiter-McLaughlin (RM) effect in some of the cross-correlation residuals. As shown in the CC residual map especially for Fe I in Fig. 7, the RM effect covers some part of velocities, where we expect the signal coming from the planet and, in consequence, in the final K_p maps and S/N plots, it can block or mimic the possible planetary signal. Removing this effect is a crucial step in the analysis. We applied two different methods to deal with this signal.

In the first case, we masked the region in the stellar rest frame, where the RM appears - a region between -10 and 10 km s⁻¹. We note that for all pixels in this region, the value is assumed to be 0 since the CC values are co-added in the next step and removing them completely was not necessary.) Then we followed the steps described in Sect. 5 by co-adding the in-transit data and calculating the S/N plots. We masked the same regions for all of the studied species, even for the species where the RM effect was not detected by eye. The S/N plots after masking are shown by the purple line in the right columns of Figs. 7 and 8 for 1900 K, and Figs. A.5 and A.6 for 4000 K.

In the second case, we modeled the RM effect together with CLV Yan et al. (2015) and Yan & Henning (2018). First we created a high-resolution stellar spectrum model using the Turbospectrum2019 code (Plez 2012), together with VALD line list assuming stellar parameters from Table 1 and PHOENIX (Husser et al. 2013) stellar model for $T_{eff} = 5750$ K, $\log g = 4$, and $[Fe/H] = 0.5$. The models account for the fact that at each orbital phase, the planet covers a different region of the star with different limb-darkening and Doppler effect. Next, we divided the modeled spectrum by the stellar spectra computed outside the transit. This ensured that the stellar spectra from all regions of the star were included in the final spectra. The remaining sig-

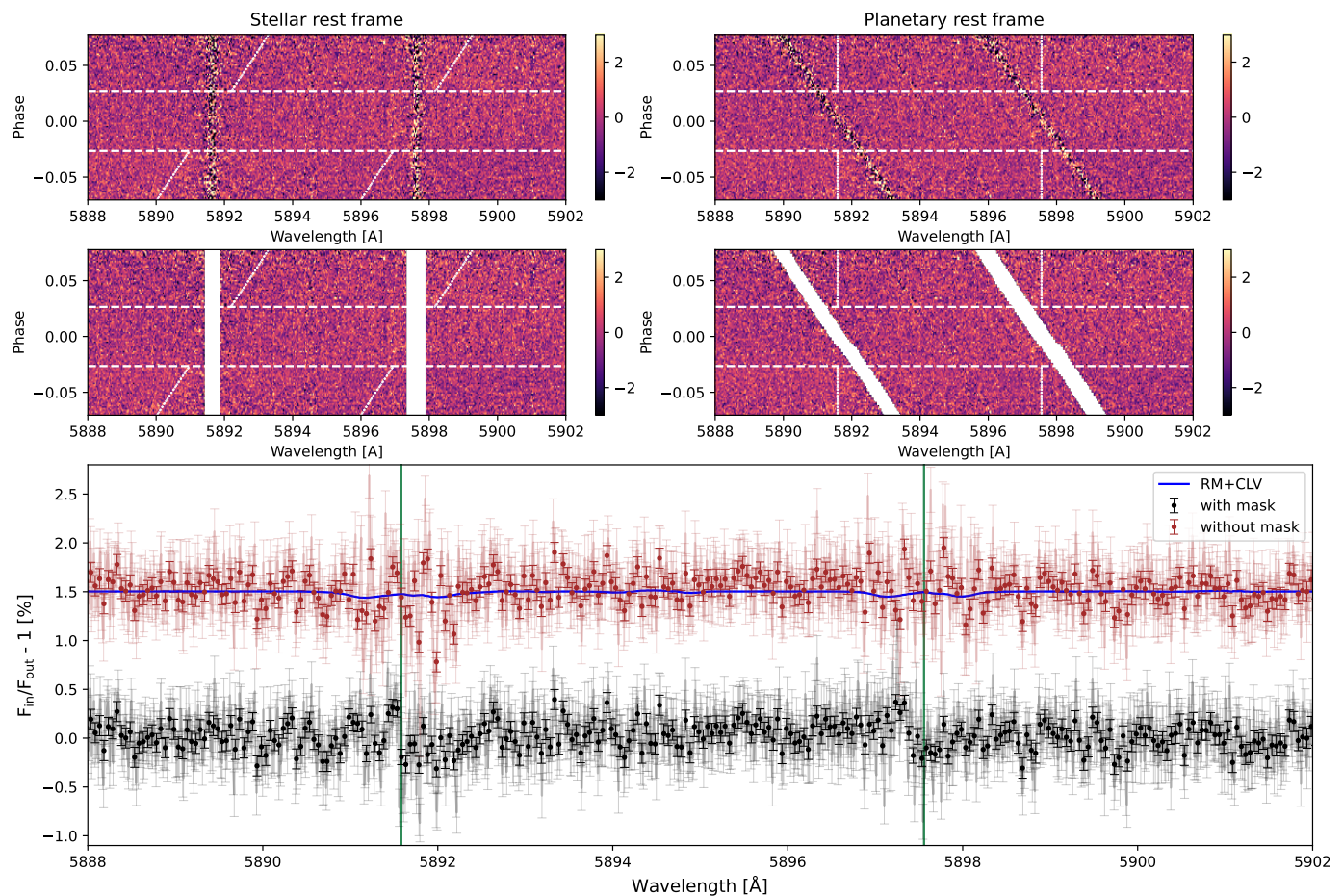


Fig. 5: 2D map of the individual transmission spectra around the Na I doublet lines of WASP-122b (top) in the stellar (left) and planetary (right) rest frame. Middle panel shows the same as the top panels, but masking the stellar signal of the Na I doublet lines (presented mask size ± 0.2 Å). Bottom panel gives the transmission spectrum computed by combining the data between the first and fourth contacts of the transit, indicated in the top panel. The red plot was computed without masking the stellar Na I lines, and the black plot with masking of these lines. Blue line represents the RM and CLV effects model. We have chosen not to show the TS after removal since the effect is marginal. The green vertical lines indicate the laboratory position of the Na I doublet lines.

nal is the RM effect. The modeled RM was convolved to the resolution of the spectrograph and cross-correlated with the atomic and molecular models described in Sect. 5. In addition, the models were scaled by the S/N of each exposure around Na I doublet.

As an example, in Fig. 6 we present the final computed RM model for Fe I. Since the S/N of the observations was not stable during the observations and WASP-122 is a slowly rotating star, the RM effect, in some of the spectra, was not detected or detected with low strength (see CC residual plots in Fig. 6). The final removal will indeed correct the RM effect in the spectra with the higher S/N but will add an additional signal in the spectra where the RM effect was not detected since the effects were not scaled by the S/N of the observations. In this case, we decided not to proceed with further analysis and did not apply this correction.

5.2. Cross-correlation results

The results of the cross-correlation analysis are shown in the Figs. 7 and 8. In the left panels, we present the cross-correlation residual maps for each of the studied species, without masking the RM effect. In the case of the H₂O, we decided to mask the regions where the atmospheric water was detected and was not

sufficiently corrected by the Molecfit code. In the second column, we show the significance maps (K_p maps), for the case without masking the RM effect. In the last column, we present S/N plots for the literature K_p . In the S/N plots, due to the fact that in some of the results we detected the RM effect (which partially lies in the regions where we would expect the signal from the planet), we show two plots. One represents the results without any correction and the second illustrates the results after we masked the region where the RM affects the data. We present the plots with masks for all the species studied, including those where the RM is not visible by eye. In all cases, we did not detect any significant signal coming from the planetary atmosphere. We present the masked plots for all the species studied, including those where the RM is not visible.

5.3. Measurement of upper limits - Injection of the signal

To measure the upper limits of the non-detections, in the case of transmission spectroscopy studies around single lines, we calculated the one-pixel dispersion of the detection. The calculation was based on the standard deviation of the transmission spectrum away from the studied line for a band of 10 Å. We assumed the upper limit to be 3σ . The calculated upper limits for the cor-

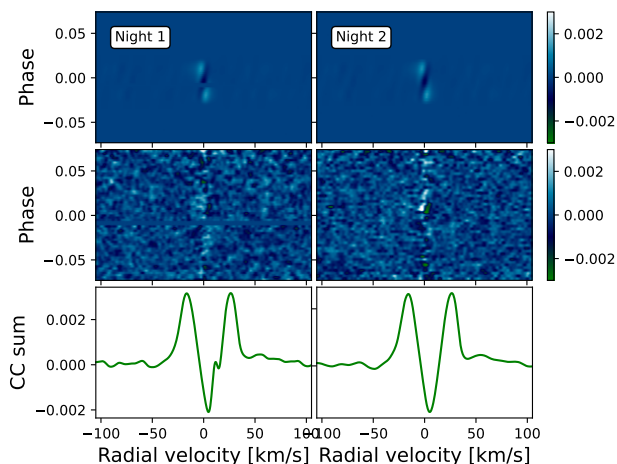


Fig. 6: Modeled RM+CLV effects for Fe I for Night 1 and Night 2. In the top plots, we present the modeled RM+CLV effects after cross-correlation with the model of Fe I. In the middle plots, we show the cross-correlation residual plots for Night 1 and Night 2 separately in order to compare the shape of the modeled RM+CLV effects. In the bottom panels, we present the CC, after summing the in-transit data of the RM effect for $K_p = 185 \text{ km s}^{-1}$. The feature in the RM+CLV model of Night 1 is due to a gap in the data during the observations.

responding lines can be found in Table 4. These values represent the minimum absorption level that can be detected using dataset from this work.

Table 4: Upper limit of 3σ for the detection of H α , H β , Na D1 & D2, and Li I.

Species	3σ [%]
H α	0.31
H β	0.48
Na D1 & D2	0.69
Li I	0.30

Following Hoeijmakers et al. (2020), Allart et al. (2017, 2020), and Casasayas-Barris et al. (2022) in order to calculate the upper limits of the detection using the cross-correlation method we injected synthetic atmospheric signal into the observational data at 200 km s^{-1} , away from the expected signal from the planetary atmosphere. In this step, the lines in the models were broadened considering the resolution of the spectrograph using `instrBroadGaussFast` routine from `PyAstronomy` (Czesla et al. 2019), the rotation of the tidally locked planet ($v_{rot} = 4.6 \text{ km s}^{-1}$) and the changes in the radial velocity during the exposure (2.3 km s^{-1} for 300 s exposure and 3.1 km s^{-1} for 400 s exposure) using `fastRotBroad` routine from `PyAstronomy`. The models were injected into the in-transit spectra with the radial velocity shift which corresponds to the expected velocity of the planet in each of the orbital phases and 200 km s^{-1} shift. The injected atmospheric models were calculated for the temperature of the planet (T_{eq}). In the final step, we cross-correlated the data with the binary mask of each of the studied atoms and molecules.

Our final 3σ upper limits, presented in Table 5, were calculated after cross-correlating the data with the binary mask of the studied atoms and molecules. For each of the species, we cre-

ated the binary mask using previously calculated models with `PetitRADTRANS` for 1904 K by choosing the strongest lines, setting a strength minimum of 0.002%. In contrast to the method presented by Casasayas-Barris et al. (2022), where only significant numbers of lines were used to calculate the upper limits, we used all the lines in the models. All of the chosen lines were given a value of 1, while the rest were set to 0. The number of lines used for each model can be found also in Table 5. The one-pixel dispersion was calculated as the standard deviation of the cross-correlation residuals for theoretical K_p , and velocities between $\pm 100 \text{ km s}^{-1}$, in the regions where we expect the atmospheric signal. We present two values, one calculated for the cross-correlation residuals with all the regions and the second after masking the regions where the Rossiter-McLaughlin effect has an impact. The values represent a minimum level of absorption which is needed to detect species using the cross-correlation method.

For all the studied species, we were not able to recover the injected signal with the strength of the theoretical expected signal; thus, we did not calculate the line upper limit, as presented in Allart et al. (2017, 2020) and Casasayas-Barris et al. (2022). To carry out an additional recovery test, we injected the models with the strengths of 2x, 4x, and ten times the expected signals. In the case of H $_2$ O and FeH, we were not able to recover any injected signal, which is probably related to the weak lines for those species at those temperatures in the visible part of the spectrum. For Ca I, Cr I, V I, and Y I, we were able to recover two times the signal with a low significance, as well as four times the signal with a high level of significance. For the rest of the species, we recovered the two times and four times signals with high significance. The S/N plots after injecting different signals can be found in Figs. A.7 and A.8.

Table 5: Upper limits of the cross-correlation detection, were calculated for the combination of the nights. A number of lines calculated for the strongest lines, with the strength of the lines: 0.002 %.

Species	Nr of lines	3σ without / with mask [ppm]
Ca I	48	271/255
Cr I	82	375/336
Fe I	176	385/335
FeH	171	241/228
H $_2$ O	332	275/269
K I	42	268/249
Na I	22	311/253
Ti I	334	375/359
TiO-Exomol	1081	254/243
TiO-Plez	1082	293/274
V I	169	295/273
VO	1076	285/264
YI	41	278/265

6. Discussion and conclusions

In this work, we study two nights of high-resolution observations of WASP-122b with the ESPRESSO spectrograph. By analyzing the Rossiter-McLaughlin effect, we were able to determine that WASP-122b is an aligned planet with an obliquity of $\lambda = 0.09^{+0.88}_{-0.90}$ deg. The results are consistent with the trend of planets orbiting stars with $T_{eff} < 6200 \text{ K}$ which show a tendency to be aligned (Winn 2010). More details are given in Fig. 4. Our $v \sin i$

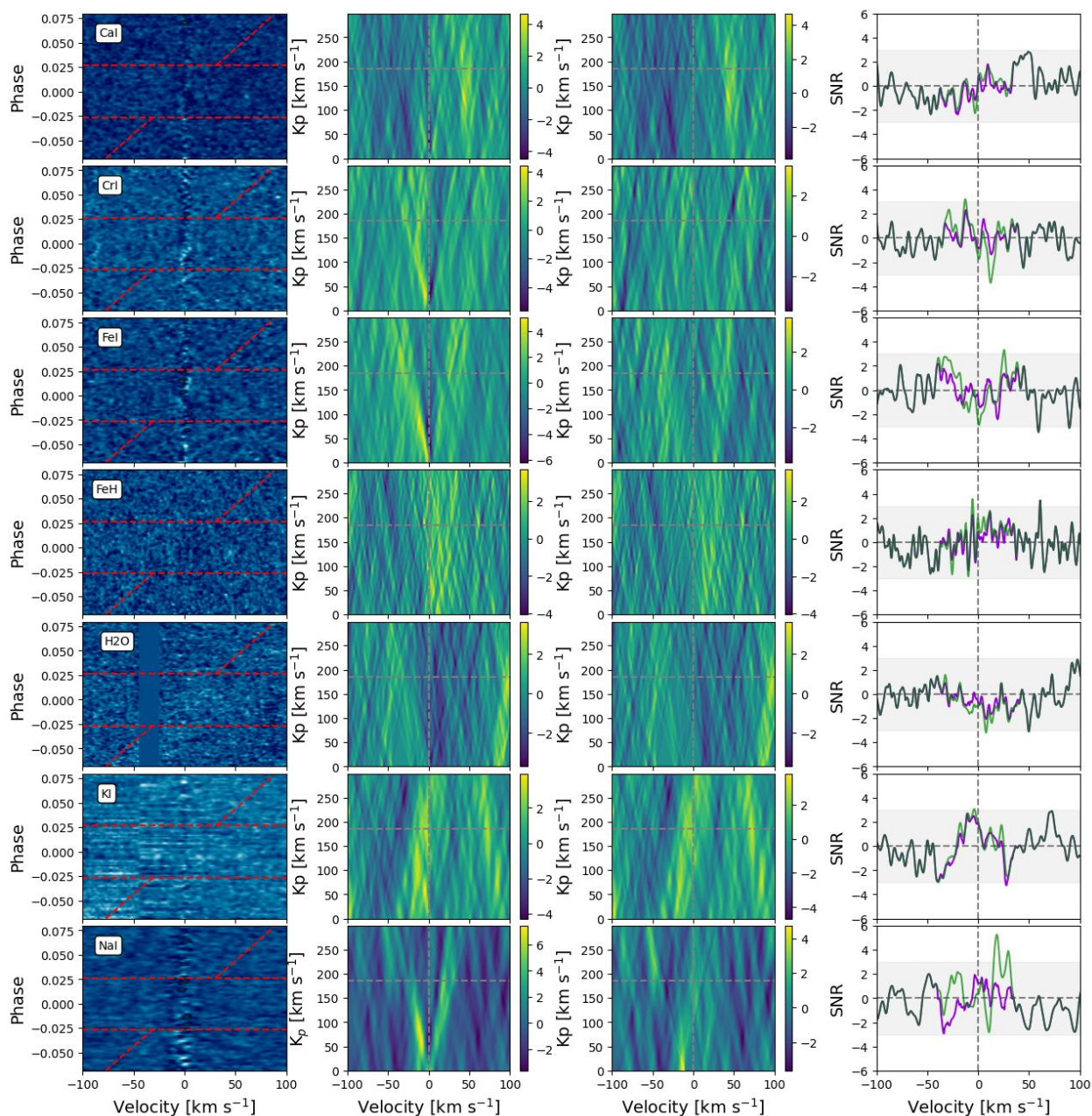


Fig. 7: Cross-correlation results for WASP-122b for Ca I, Cr I, Fe I, FeH, H₂O, K I, and Na I. For each of the species, we present the following plots. First column: Residual map before masking the RM effect, where the red horizontal lines represent the beginning and end of the transit and the red tilted line represents the expected velocity of the planet. Second column: K_p map calculated for a range of 0 to 300 km s⁻¹, the theoretical K_p of the planets is represented by a gray horizontal line. Expected signal from the planet should be detected at $K_p = 185$ km s⁻¹ and radial velocity 0 km s⁻¹. Third column: Same as the second column but after masking the RM effect. Fourth column: S/N plot for theoretical K_p value. The green plot is the raw S/N plot and the purple plot is S/N after masking the regions where the RM effect appears. The horizontal gray dashed line represents S/N = 0, and the vertical gray dashed line represents the radial velocity of 0 km/s, which is the expected position of the CC peak. The gray regions represent S/N between -3 and 3.

$= 1.84 \pm 0.08$ km s⁻¹ value is smaller than the two previously reported literature measurements of 3.3 ± 0.8 km s⁻¹ (Turner et al. 2016) and 7.7 ± 0.4 km s⁻¹ (Rodríguez et al. 2016). This difference can be explained by the larger collective area, larger wavelength range, and higher resolution of the ESPRESSO data used in our analysis than that used by Turner et al. (2016) (CYCLOPS data) and Rodríguez et al. (2016) (CORALIE data).

Additionally, to study the chemical composition of the atmosphere of WASP-122b, we used the transmission spectroscopy method. By looking at the transmission spectroscopic signal around single lines, we investigated the presence of the Na I doublet, H α , H β , and Li I. The final results show no evidence of any of the studied atoms.

Using the cross-correlation method, we searched for a list of atoms and the molecules in the atmosphere of WASP-122b: Ca I,

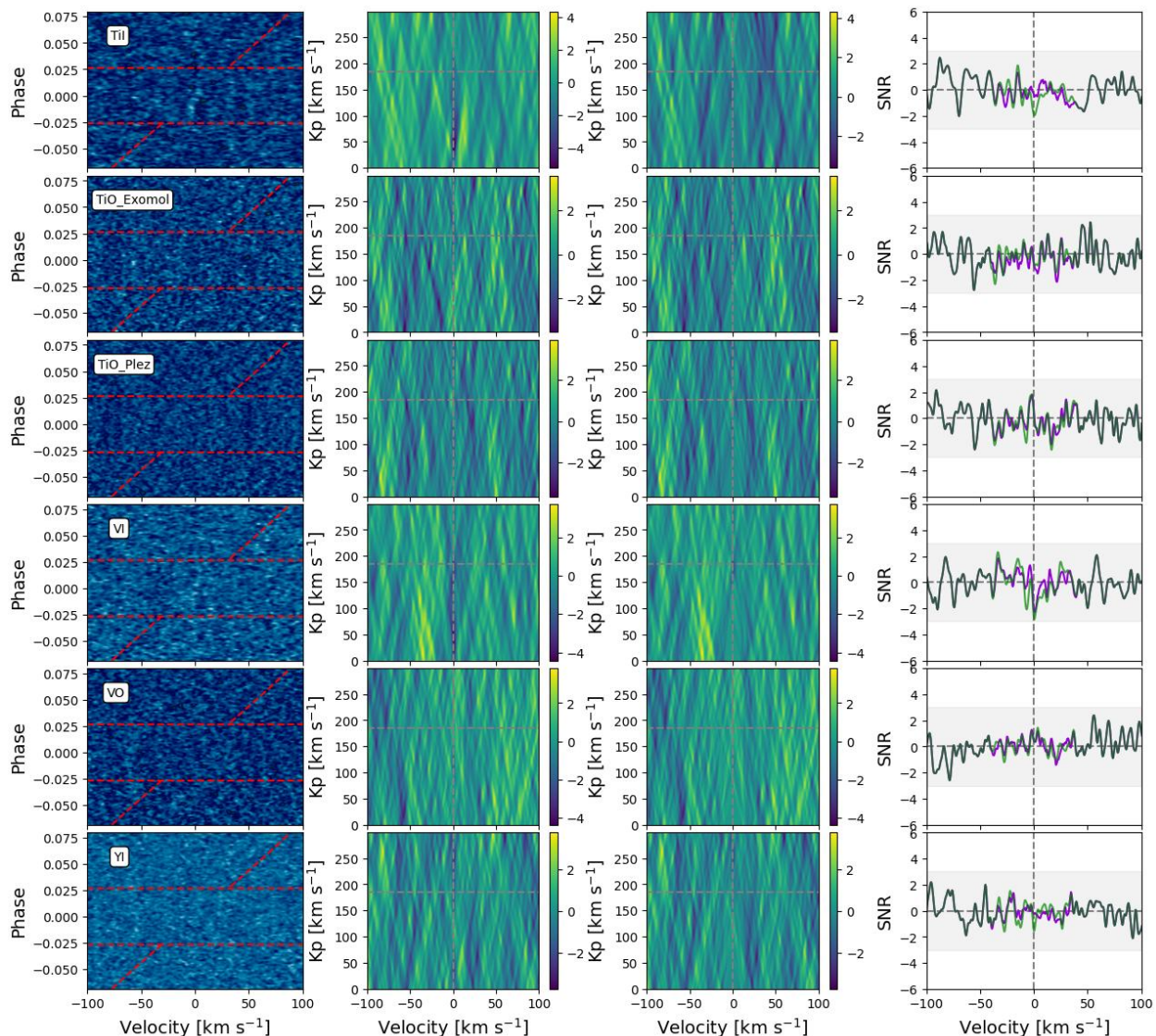


Fig. 8: Same as Fig. 7 but for Ti I, TiO (Exomol), TiO (Plez), V I, VO, and Y I.

Cr I, Fe H, Fe I, Fe II, H₂O, K I, Mg I, Na I, Ti I, TiO, V I, VO, and Y I. As in the case of single-line studies, we did not detect any signal with an S/N higher than 3σ .

The lack of detections can be explained by the absence or low abundances of all the studied species in the region of the atmosphere probed by our analysis. WASP-122b is a hot Jupiter; thus, we expect the existence of several molecules in its atmosphere, which show weak spectral lines in the visible part of the spectrum, but atomic species such as Na would also be expected. Alternatively, it is possible that the difficulties in the correction of the RM effect, which covers a broad range of the radial velocities where the planetary signal is expected, could explain these results. Additionally, the planet's atmosphere can be cloudy and most lines can be hidden or weakened under the cloud layer. Moreover, the low S/N of the observations makes it difficult to detect weaker signal coming from the atmosphere of this planet.

The three planets, KELT-7b ($T_{eq} = 2048 \pm 27$ K, TSM ~ 170 , $M_p = 1.28 \pm 0.18 M_J$, $R_p = 1.533^{+0.046}_{-0.047} R_J$, Bieryla et al. 2015), WASP-19b ($T_{eq} = 2077 \pm 34$ K, TSM ~ 170 , $M_p = 1.139^{+0.03}_{-0.02} M_J$, $R_p = 1.410^{+0.017}_{-0.013} R_J$, Mancini et al. 2013), and WASP-74b ($T_{eq} = 1910 \pm 40$, TSM ~ 160 , $M_p = 0.95 \pm 0.06$, $R_p = 1.56 \pm$

$0.06 R_J$, West et al. 2016) are of a similar class to WASP-122b (TSM ~ 180) in terms of all T_{eq} , radius, mass, and TSM. The atmosphere of KELT-7b was previously studied with the high-resolution spectrographs HORuS and HARPS-N showing no atmospheric signature (Stangret et al. 2022, Tabernero et al. 2022), while using the *Hubble* Space Telescope (HST), Changeat et al. 2022 presented the detection of H₂O and H- in the atmosphere of this planet. The atmosphere of WASP-19b has been studied by several groups using both space- and ground-based spectrographs, showing the presence of TiO and H₂O (Huitson et al. 2013, Sing et al. 2016, Sedaghati et al. 2017, Sedaghati et al. 2021, Changeat et al. 2022). In the case of WASP-74b, observations with HST revealed the presence of H₂O and CH₄ (Changeat et al. 2022). Since all of those planets are in transition between hot and ultra-hot Jupiters, we can presume that for some of the atoms and molecules, it is extremely difficult to probe their atmospheric composition using high-resolution spectrographs since the abundance of those species can be in transition between natural and ionized states as well as undergoing dissociation.

Future studies should focus on observations using the near-infrared part of the spectrum such as CRIFES⁺, as well as space

observations from HST or JWST. These observations could detect molecules such as water, CH₄, and a possible cloud layer, which could then be used for the atmospheric retrieval and help constrain the temperature of the upper atmosphere.

Acknowledgements. M.S. acknowledges the support of the PRIN INAF 2019 through the project “HOT-ATMOS” and INAF GO Large Grant 2023 GAPS-2. JIGH acknowledge financial support from the Spanish Ministry of Science and Innovation (MICINN) project PID2020-117493GB-I00.; We acknowledge funding from the European Research Council under the European Union’s Horizon 2020 research and innovation program under grant agreement No. 694513. This work was financed by Portuguese funds through FCT - Fundação para a Ciência e a Tecnologia in the framework of the project 2022.04048.PTDC (Phi in the Sky). CJM also acknowledges FCT and POCH/FSE (EC) support through Investigador FCT Contract 2021.01214.CEECIND/CP1658/CT0001.; This work was supported by Fundação para a Ciência e a Tecnologia (FCT) and Fundo Europeu de Desenvolvimento Regional (FEDER) via COMPETE2020 through the research grants UIDB/04434/2020, UIDP/04434/2020, 2022.06962.PTDC. O.D.S.D. is supported in the form of work contract (DL 57/2016/CP1364/CT0004) funded by FCT.;NCS was acknowledges the funding by the European Union (ERC, FIERCE, 101052347). Views and opinions expressed are however those of the author(s) only and do not necessarily reflect those of the European Union or the European Research Council. Neither the European Union nor the granting authority can be held responsible for them. This work was supported by FCT - Fundação para a Ciência e a Tecnologia through national funds and by FEDER through COMPETE2020 - Programa Operacional Competitividade e Internacionalização by these grants: UIDB/04434/2020; UIDP/04434/2020.; This project has received funding from the Swiss National Science Foundation for project 200021_200726. It has also been carried out within the framework of the National Centre of Competence in Research PlanetS supported by the Swiss National Science Foundation under grant 51NF40_205606. The authors acknowledge the financial support of the SNSF; R. A. is an SNSF Postdoctoral Fellow and acknowledges the SNSF support under the Post-Doc Mobility grant P500PT_222212. This work was funded by the Institut Trotier de Recherche sur les Exoplanètes (iREx), and R.A. acknowledges support from the Trotier Family Foundation. This work has been carried out within the framework of the National Centre of Competence in Research PlanetS, supported by the Swiss National Science Foundation.; E.H.-C. acknowledges support from grant PRE2020-094770 under project PID2019-109522GB-C51 funded by the Spanish Ministry of Science and Innovation / State Agency of Research, MCIN/AEI/10.13039/501100011033, and by ‘ERDF, A way of making Europe’; This work made use of PyAstronomy (Czesla et al. 2019) and of the VALD database, operated at Uppsala University, the Institute of Astronomy RAS in Moscow, and the University of Vienna. ARoME code is publicly available at <http://www.astro.up.pt/resources/arome/>. The Python translation of ARoME was made by A. Santerne.

References

Addison, B. C., Wang, S., Johnson, M. C., et al. 2018, *AJ*, 156, 197
 Allart, R., Lovis, C., Pino, L., et al. 2017, *A&A*, 606, A144
 Allart, R., Pino, L., Lovis, C., et al. 2020, *A&A*, 644, A155
 Alonso-Floriano, F. J., Sánchez-López, A., Snellen, I. A. G., et al. 2019a, *A&A*, 621, A74
 Alonso-Floriano, F. J., Snellen, I. A. G., Czesla, S., et al. 2019b, *A&A*, 629, A110
 Arcangeli, J., Désert, J.-M., Line, M. R., et al. 2018, *ApJ*, 855, L30
 Asplund, M., Grevesse, N., Sauval, A. J., & Scott, P. 2009, *ARA&A*, 47, 481
 Bieryla, A., Collins, K., Beatty, T. G., et al. 2015, *AJ*, 150, 12
 Birkby, J. L., de Kok, R. J., Brogi, M., Schwarz, H., & Snellen, I. A. G. 2017, *AJ*, 153, 138
 Borsa, F., Fossati, L., Koskinen, T., Young, M. E., & Shulyak, D. 2021, *Nature Astronomy* [arXiv:2112.12059]
 Boucher, A., Darveau-Bernier, A., Pelletier, S., et al. 2021, *AJ*, 162, 233
 Boucher, A., Lafrenière, D., Pelletier, S., et al. 2023, *MNRAS*, 522, 5062
 Boué, G., Montalto, M., Boisse, I., Oshagh, M., & Santos, N. C. 2013, *A&A*, 550, A53
 Bourrier, V., Lovis, C., Cretignier, M., et al. 2021, *A&A*, 654, A152
 Brogi, M. & Line, M. R. 2019, *AJ*, 157, 114
 Brogi, M., Snellen, I. A. G., de Kok, R. J., et al. 2012, *Nature*, 486, 502
 Cabot, S. H. C., Madhusudhan, N., Hawker, G. A., & Gandhi, S. 2019, *MNRAS*, 482, 4422
 Casasayas-Barris, N., Borsa, F., Palle, E., et al. 2022, *A&A*, 664, A121
 Casasayas-Barris, N., Palle, E., Nowak, G., et al. 2017, *A&A*, 608, A135
 Casasayas-Barris, N., Palle, E., Stangret, M., et al. 2021, *A&A*, 647, A26
 Casasayas-Barris, N., Pallé, E., Yan, F., et al. 2018, *A&A*, 616, A151
 Casasayas-Barris, N., Pallé, E., Yan, F., et al. 2020, *A&A*, 635, A206

Cauley, P. W., Shkolnik, E. L., Ilyin, I., et al. 2019, *AJ*, 157, 69
 Changeat, Q., Edwards, B., Al-Refaie, A. F., et al. 2022, *ApJS*, 260, 3
 Chen, G., Casasayas-Barris, N., Pallé, E., et al. 2020a, *A&A*, 642, A54
 Chen, G., Casasayas-Barris, N., Pallé, E., et al. 2020b, *A&A*, 635, A171
 Chiavassa, A. & Brogi, M. 2019, *A&A*, 631, A100
 Cristo, E., Esparza Borges, E., Santos, N. C., et al. 2024, *A&A*, 682, A28
 Cristo, E., Santos, N. C., Demangeon, O., et al. 2022, *A&A*, 660, A52
 Czesla, S., Schröter, S., Schneider, C. P., et al. 2019, *PyA: Python astronomy-related packages*, *Astrophysics Source Code Library*, record ascl:1906.010
 Edwards, B., Changeat, Q., Yip, K. H., et al. 2021, *MNRAS*, 504, 5671
 Esposito, M., Covino, E., Desidera, S., et al. 2017, *A&A*, 601, A53
 Foreman-Mackey, D., Hogg, D. W., Lang, D., & Goodman, J. 2013, *PASP*, 125, 306
 Giacobbe, P., Brogi, M., Gandhi, S., et al. 2021, *Nature*, 592, 205
 Guilluy, G., Andretta, V., Borsa, F., et al. 2020, *A&A*, 639, A49
 Guilluy, G., Sozzetti, A., Brogi, M., et al. 2019, *A&A*, 625, A107
 Hoeijmakers, H. J., Ehrenreich, D., Heng, K., et al. 2018, *Nature*, 560, 453
 Hoeijmakers, H. J., Ehrenreich, D., Kitzmann, D., et al. 2019, *A&A*, 627, A165
 Hoeijmakers, H. J., Seidel, J. V., Pino, L., et al. 2020, *A&A*, 641, A123
 Holt, J. R. 1893, *Astronomy and Astro-Physics (formerly The Sidereal Messenger)*, 12, 646
 Huitson, C. M., Sing, D. K., Pont, F., et al. 2013, *MNRAS*, 434, 3252
 Husser, T. O., Wende-von Berg, S., Dreizler, S., et al. 2013, *A&A*, 553, A6
 Ishizuka, M., Kawahara, H., Nugroho, S. K., et al. 2021, *AJ*, 161, 153
 Kausch, W., Noll, S., Smette, A., et al. 2015, *A&A*, 576, A78
 Kempton, E. M. R., Bean, J. L., Louie, D. R., et al. 2018, *PASP*, 130, 114401
 Khalafnejad, S., Molaverdikhani, K., Blecic, J., et al. 2021, *A&A*, 656, A142
 Kraft, R. P. 1967, *ApJ*, 150, 551
 Line, M. R., Brogi, M., Bean, J. L., et al. 2021, *Nature*, 598, 580
 Lockwood, A. C., Johnson, J. A., Bender, C. F., et al. 2014, *ApJ*, 783, L29
 Mancini, L., Ciceri, S., Chen, G., et al. 2013, *MNRAS*, 436, 2
 McKemmish, L. K., Masseron, T., Hoeijmakers, H. J., et al. 2019, *MNRAS*, 488, 2836
 McLaughlin, D. B. 1924, *ApJ*, 60, 22
 Mollière, P., Wardenier, J. P., van Boekel, R., et al. 2019, *A&A*, 627, A67
 Nortmann, L., Lesjak, F., Yan, F., et al. 2024, arXiv e-prints, arXiv:2404.12363
 Nortmann, L., Pallé, E., Salz, M., et al. 2018, *Science*, 362, 1388
 Oshagh, M., Triana, A. H. M. J., Burdanov, A., et al. 2018, *A&A*, 619, A150
 Palle, E., Oshagh, M., Casasayas-Barris, N., et al. 2020, *A&A*, 643, A25
 Parviainen, H. & Aigrain, S. 2015, *MNRAS*, 453, 3821
 Pepe, F., Cristiani, S., Rebolo, R., et al. 2021, *A&A*, 645, A96
 Pepe, F., Mayor, M., Galland, F., et al. 2002, *A&A*, 388, 632
 Pino, L., Désert, J.-M., Brogi, M., et al. 2020, *ApJ*, 894, L27
 Plez, B. 1998, *A&A*, 337, 495
 Plez, B. 2012, *Turbospectrum: Code for spectral synthesis*, *Astrophysics Source Code Library*, record ascl:1205.004
 Rodriguez, J. E., Colón, K. D., Stassun, K. G., et al. 2016, *AJ*, 151, 138
 Rossiter, R. A. 1924, *ApJ*, 60, 15
 Salz, M., Czesla, S., Schneider, P. C., et al. 2018, *A&A*, 620, A97
 Sánchez-López, A., Alonso-Floriano, F. J., López-Puertas, M., et al. 2019, *A&A*, 630, A53
 Santos, N. C., Cristo, E., Demangeon, O., et al. 2020, *A&A*, 644, A51
 Schlesinger, F. 1910, *Publications of the Allegheny Observatory of the University of Pittsburgh*, 1, 123
 Sedaghati, E., Boffin, H. M. J., MacDonald, R. J., et al. 2017, *Nature*, 549, 238
 Sedaghati, E., MacDonald, R. J., Casasayas-Barris, N., et al. 2021, *MNRAS*, 505, 435
 Seidel, J. V., Prinoth, B., Knudstrup, E., et al. 2023, *A&A*, 678, A150
 Sing, D. K., Fortney, J. J., Nikolov, N., et al. 2016, *Nature*, 529, 59
 Smette, A., Sana, H., Noll, S., et al. 2015, *A&A*, 576, A77
 Snellen, I. A. G., de Kok, R. J., de Mooij, E. J. W., & Albrecht, S. 2010, *Nature*, 465, 1049
 Southworth, J. 2011, *MNRAS*, 417, 2166
 Stangret, M., Casasayas-Barris, N., Pallé, E., et al. 2022, *A&A*, 662, A101
 Stangret, M., Pallé, E., Casasayas-Barris, N., et al. 2021, *A&A*, 654, A73
 Tabernero, H. M., Zapatero Osorio, M. R., Allart, R., et al. 2021, *A&A*, 646, A158
 Tabernero, H. M., Zapatero Osorio, M. R., Allende Prieto, C., et al. 2022, *MNRAS*, 515, 1247
 Triard, A. H. M. J. 2018, in *Handbook of Exoplanets*, ed. H. J. Deeg & J. A. Belmonte, 2
 Turner, O. D., Anderson, D. R., Collier Cameron, A., et al. 2016, *PASP*, 128, 064401
 Wang, S., Addison, B., Fischer, D. A., et al. 2018, *AJ*, 155, 70
 Webb, R. K., Gandhi, S., Brogi, M., et al. 2022, *MNRAS*, 514, 4160
 West, R. G., Hellier, C., Almenara, J. M., et al. 2016, *A&A*, 585, A126
 Winn, J. N. 2010, in *Exoplanets*, ed. S. Seager, 55–77
 Winn, J. N., Johnson, J. A., Marcy, G. W., et al. 2006, *ApJ*, 653, L69
 Wytenbach, A., Ehrenreich, D., Lovis, C., Udry, S., & Pepe, F. 2015, *A&A*, 577, A62
 Wytenbach, A., Mollière, P., Ehrenreich, D., et al. 2020, *A&A*, 638, A87
 Yan, F., Casasayas-Barris, N., Molaverdikhani, K., et al. 2019, *A&A*, 632, A69
 Yan, F., Fosbury, R. A. E., Petr-Gotzens, M. G., Zhao, G., & Pallé, E. 2015, *A&A*, 574, A94
 Yan, F. & Henning, T. 2018, *Nature Astronomy*, 2, 714

Appendix A: Additional figures

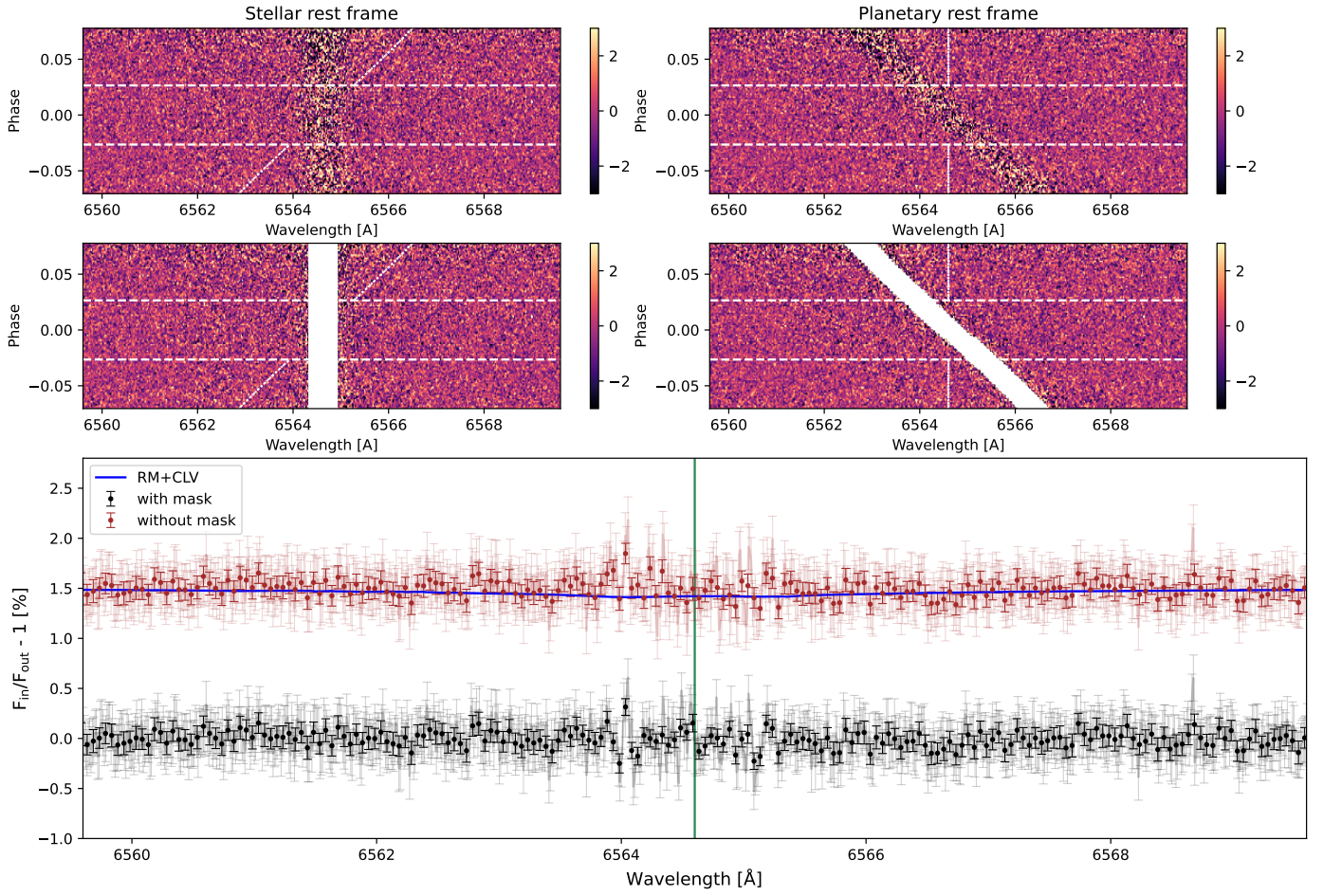


Fig. A.1: Same as Fig. 5, but for H α (presented mask size ± 0.3 Å).

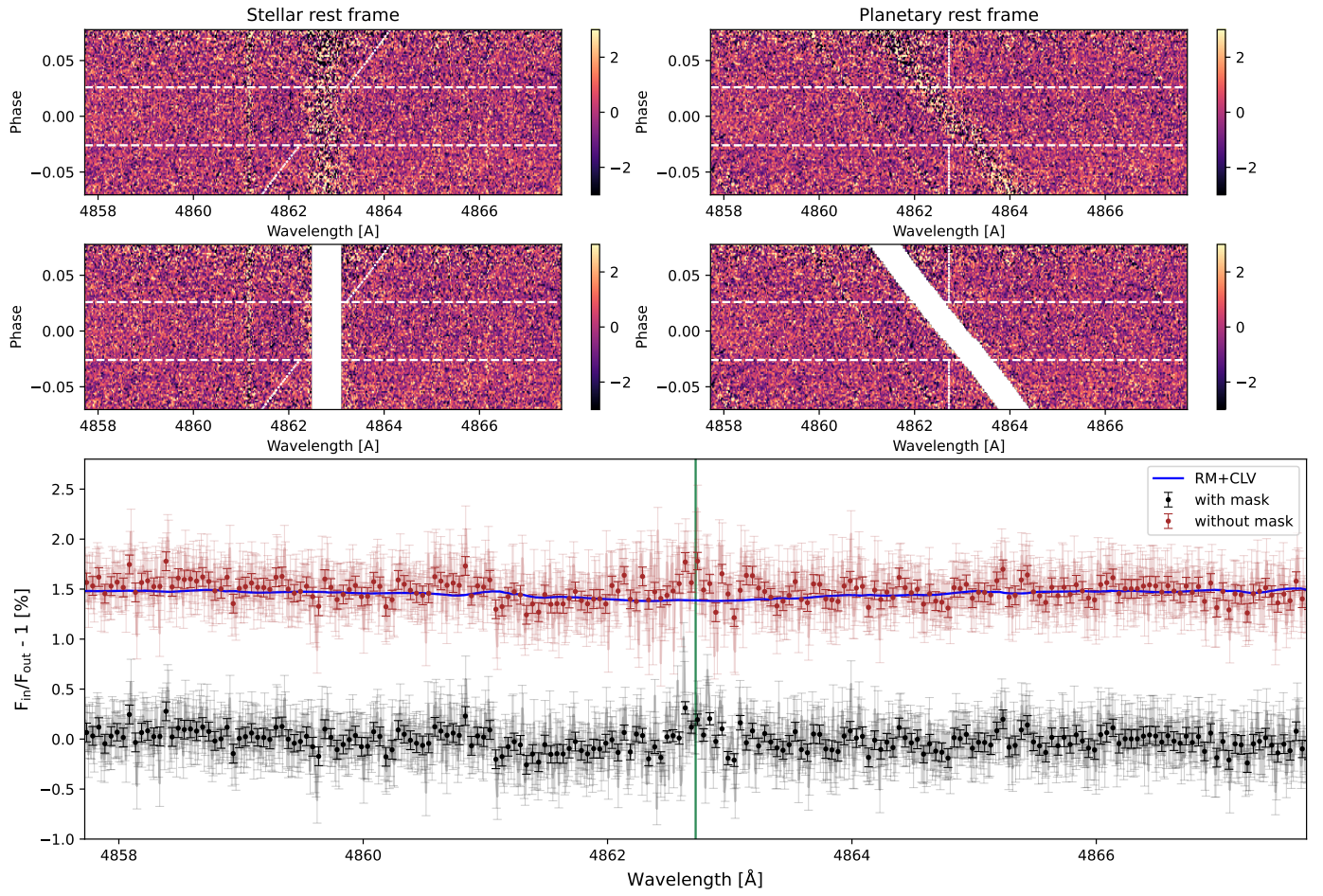


Fig. A.2: Same as Fig. 5, but for H β (presented mask size ± 0.3 Å).

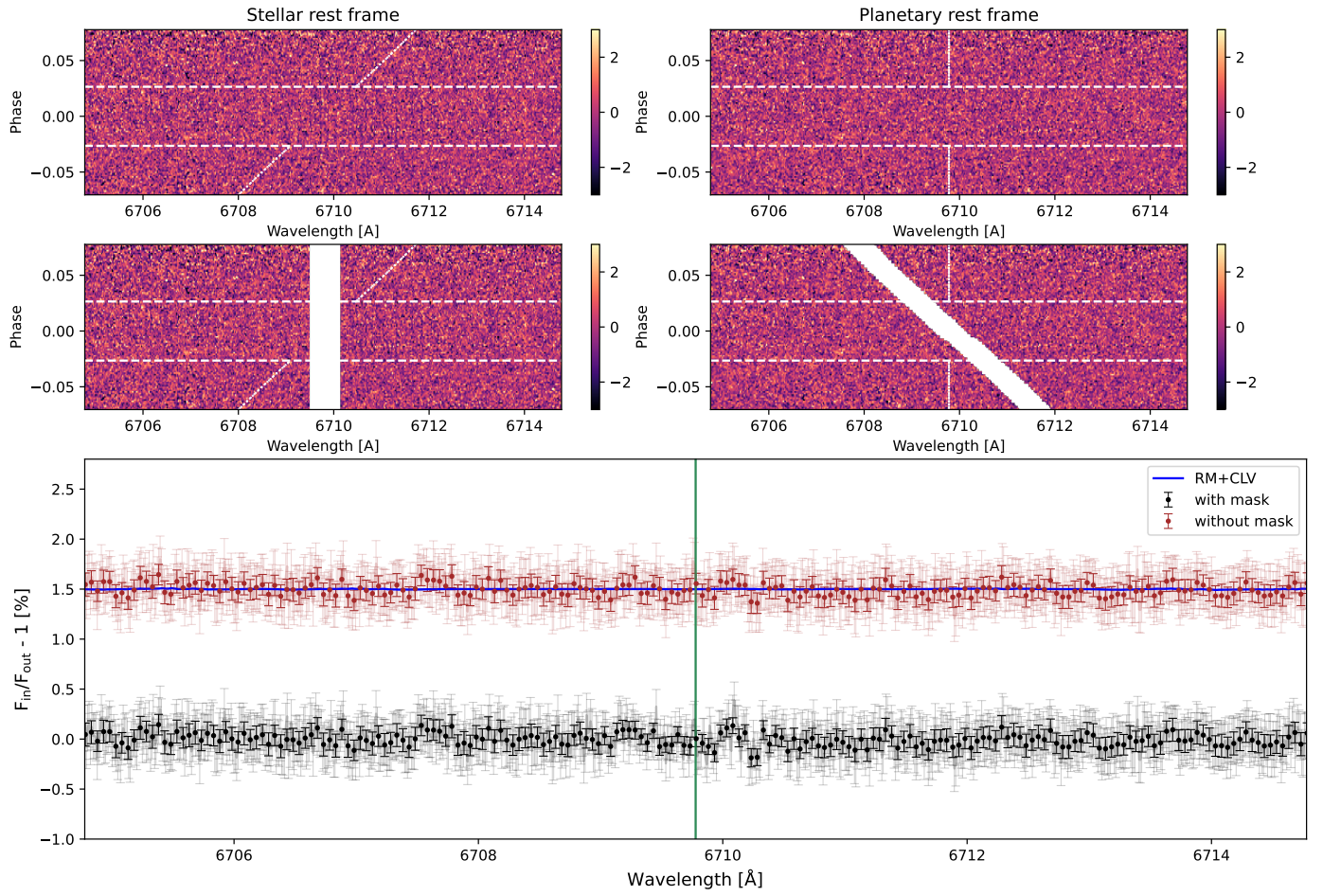


Fig. A.3: Same as Fig. 5, but for Li I (presented mask size $\pm 0.3 \text{ \AA}$).

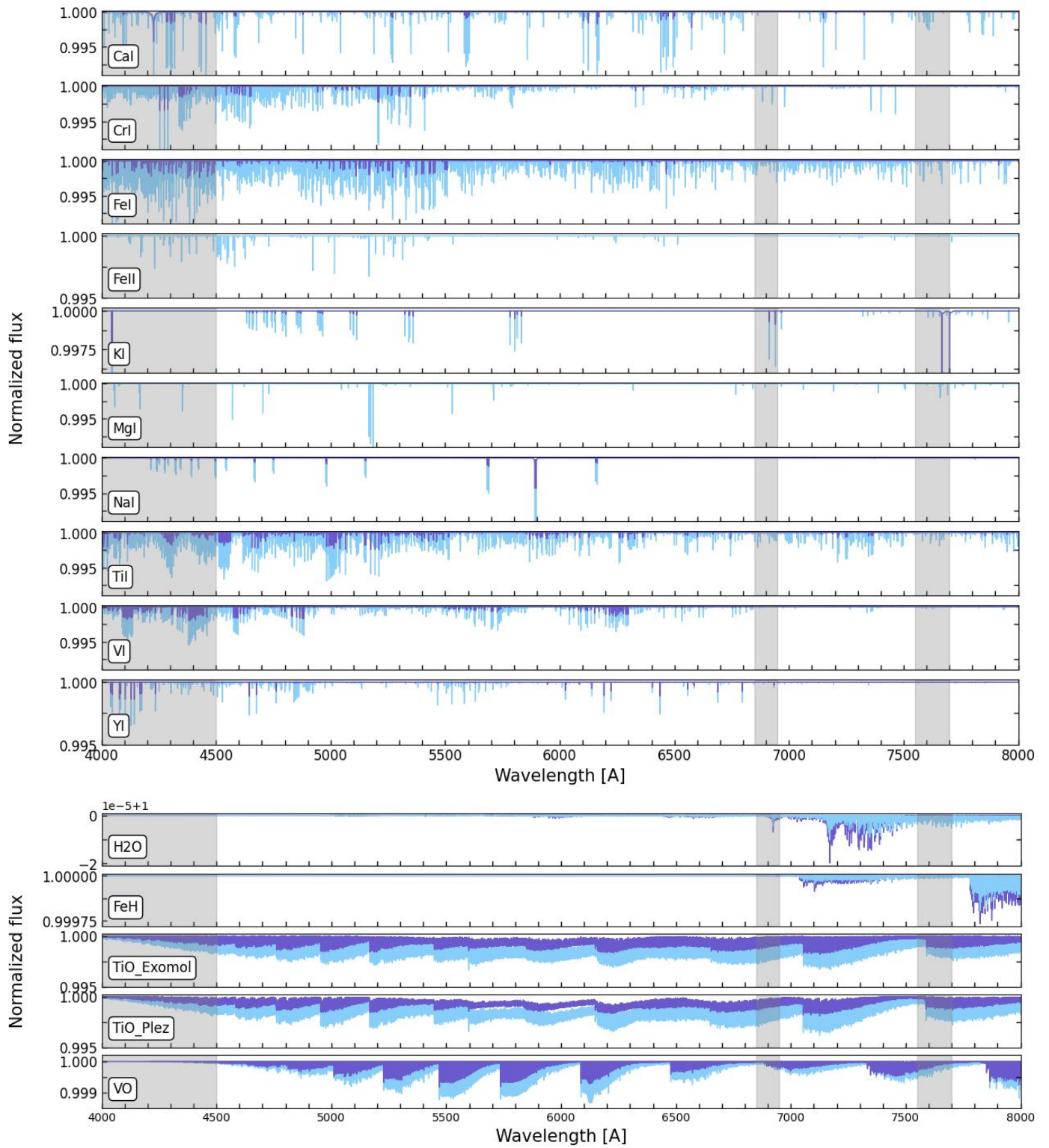


Fig. A.4: Modeled spectrum of atoms (upper panel) and molecules (bottom panel): Ca I (Kurucz), Cr I (Kurucz), FeH, Fe I (Kurucz), Fe II (Kurucz), H₂O (HITEMP), Mg I (Kurucz), Na I (Kurucz), Ti I (Kurucz), TiO (B. Plez, ExoMolOP), V I (Kurucz), VO (ExoMolOP) ,and Y I (Kurucz). Dark blue plots represent models calculated for 4000 K and light blue for 1900 K. In the case of Fe II and Mg I there are no or few spectral lines for lower temperature, in this case, we only plot the models for higher temperature. In the grey vertical regions, we show the areas of the spectrum that were not used in the cross-correlation analysis.

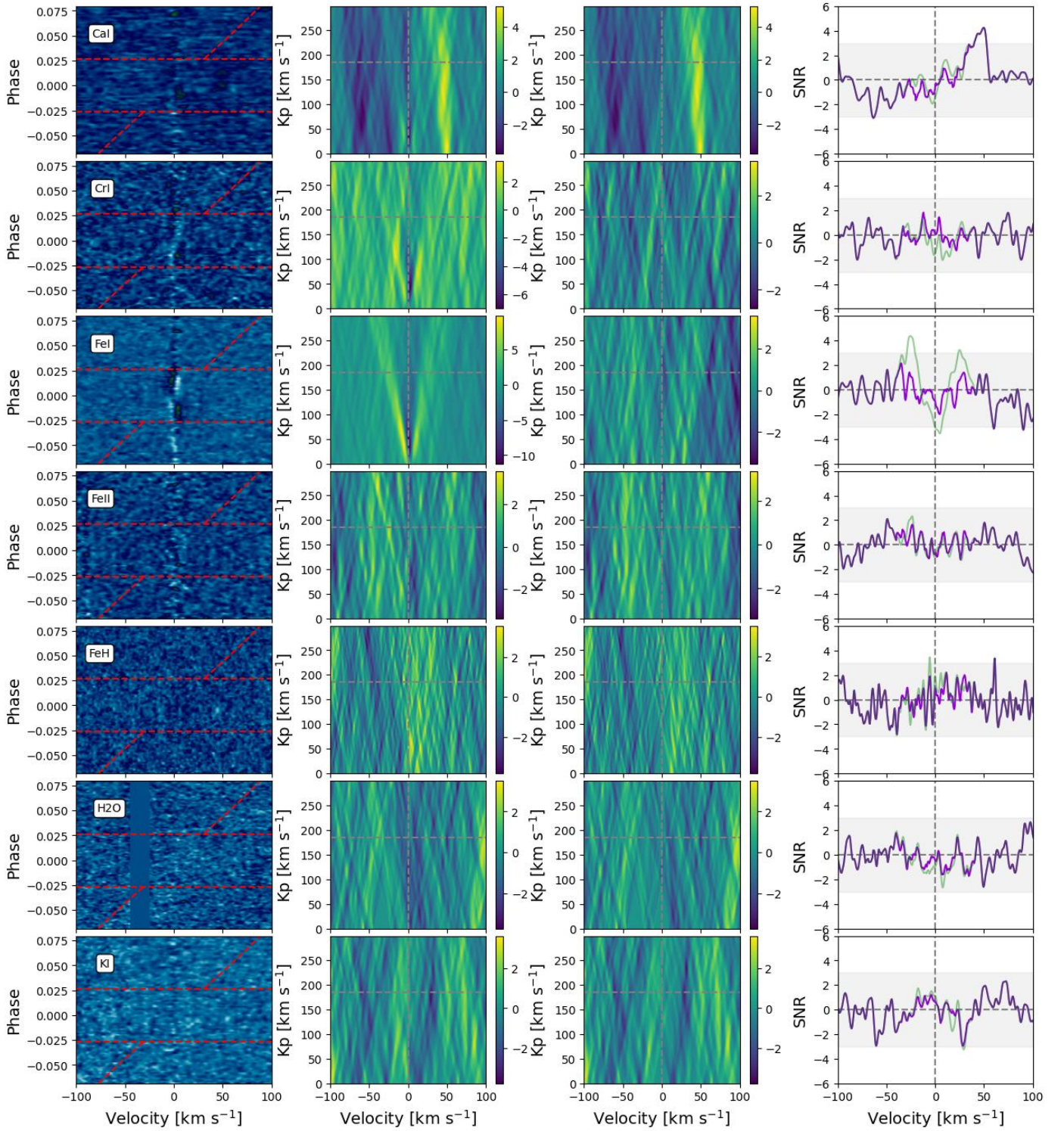


Fig. A.5: Same as Fig. 7, but for models of Ca I, Cr I, Fe I, Fe II, Fe H, H₂O, and K I calculated for temperature of 4000 K.

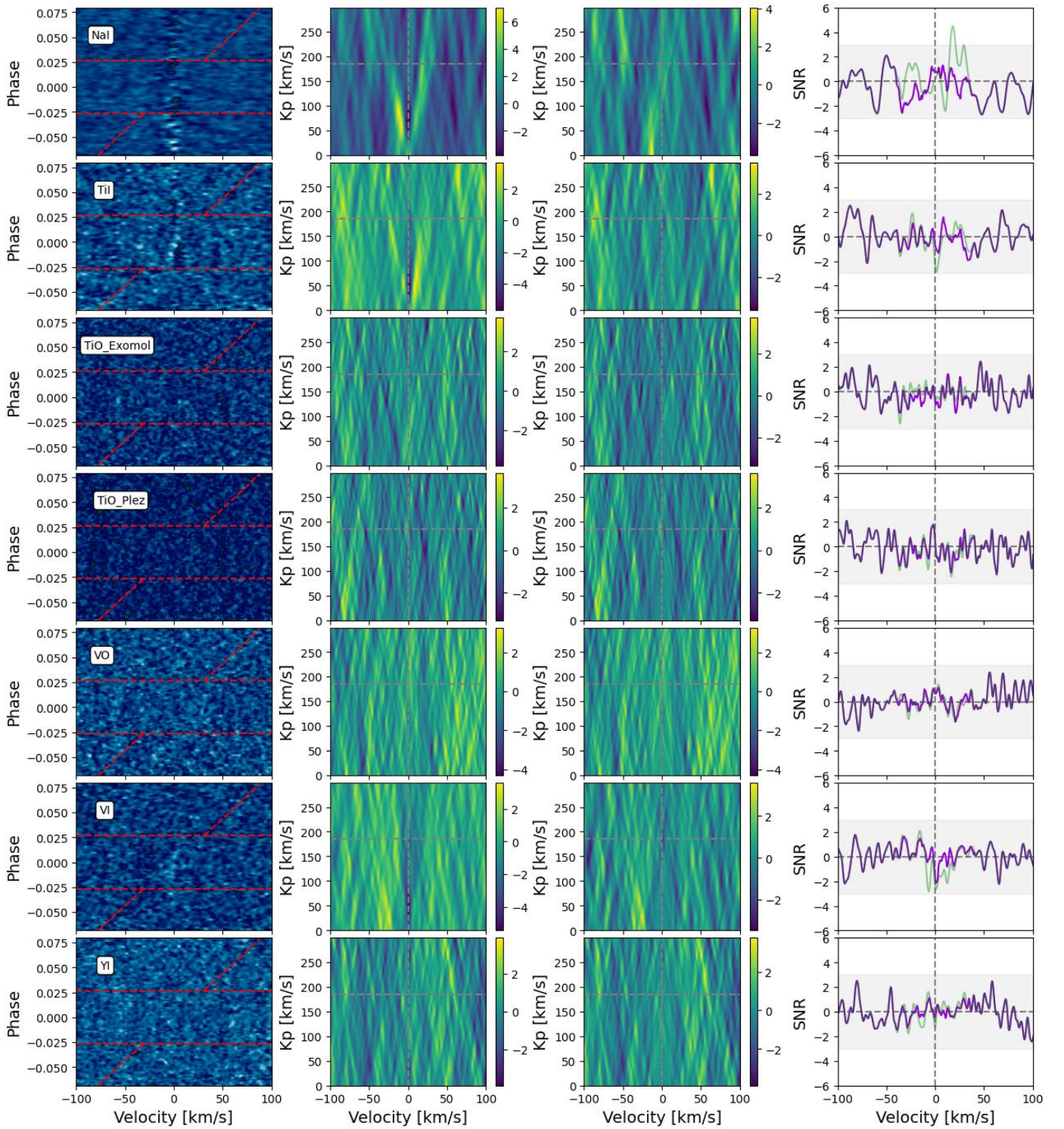


Fig. A.6: Same as Fig. 7, but for models of Na I, Ti I, TiO (Exomol), TiO (Plez), VO, V I, and Y I calculated for the temperature of 4000 K.

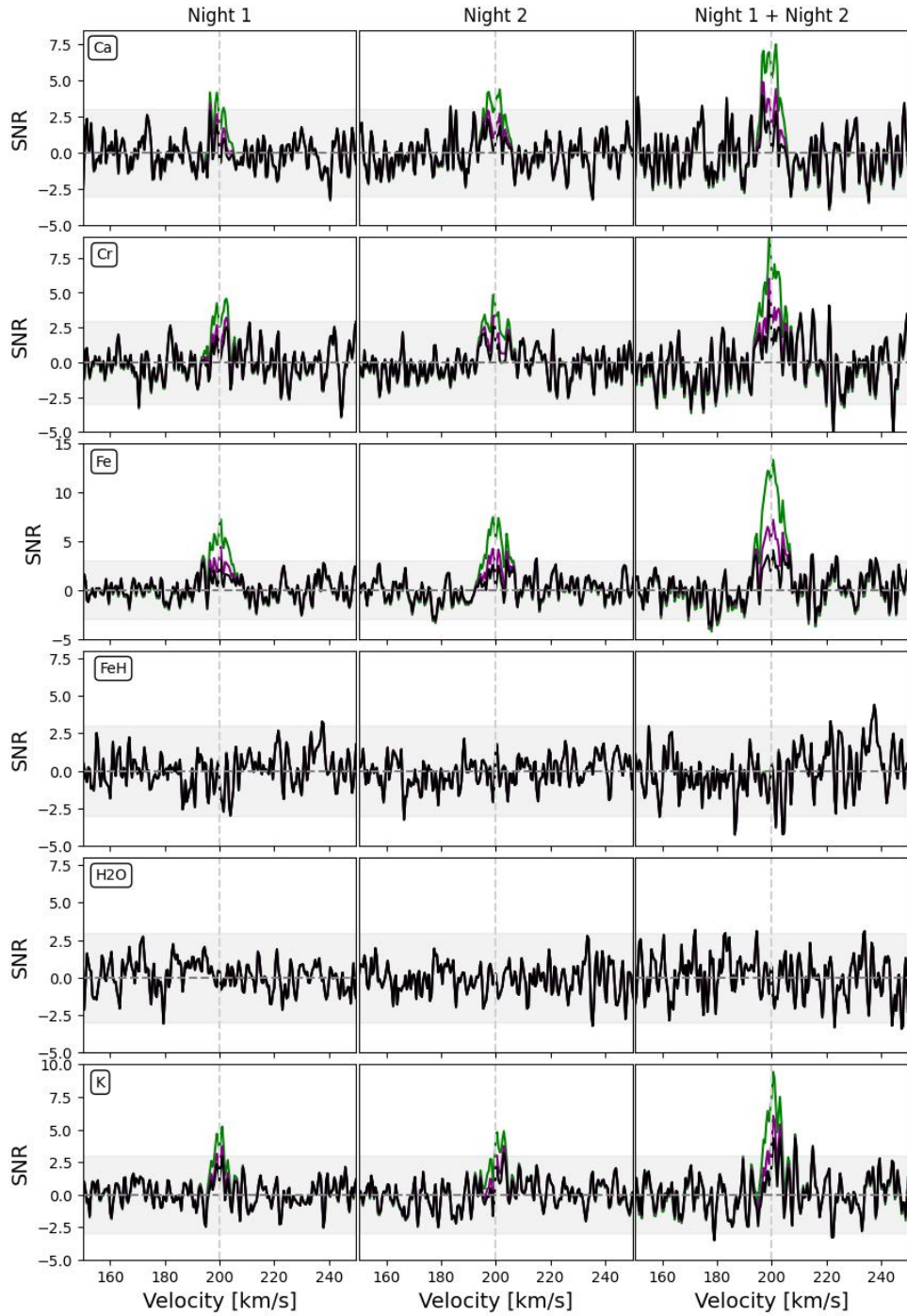


Fig. A.7: S/N plots after injecting the signal of Ca I, Cr I, Fe I, FeH, H₂O, and K I. In the first column, we present the injection of the species into the data from Night 1, in the second column into Night 2, and in the third column, we present data after combining Night 1 and Night 2. The black plots represent the injected signal with an expected strength of the signal, the purple plot with a 2x of the expected signal, and the green with a 4x strength of the injected signal. The horizontal gray dashed line represents $S/N = 0$, and the vertical gray dashed line represents the radial velocity of 0 km/s. The gray regions represent S/N between -3 and 3.

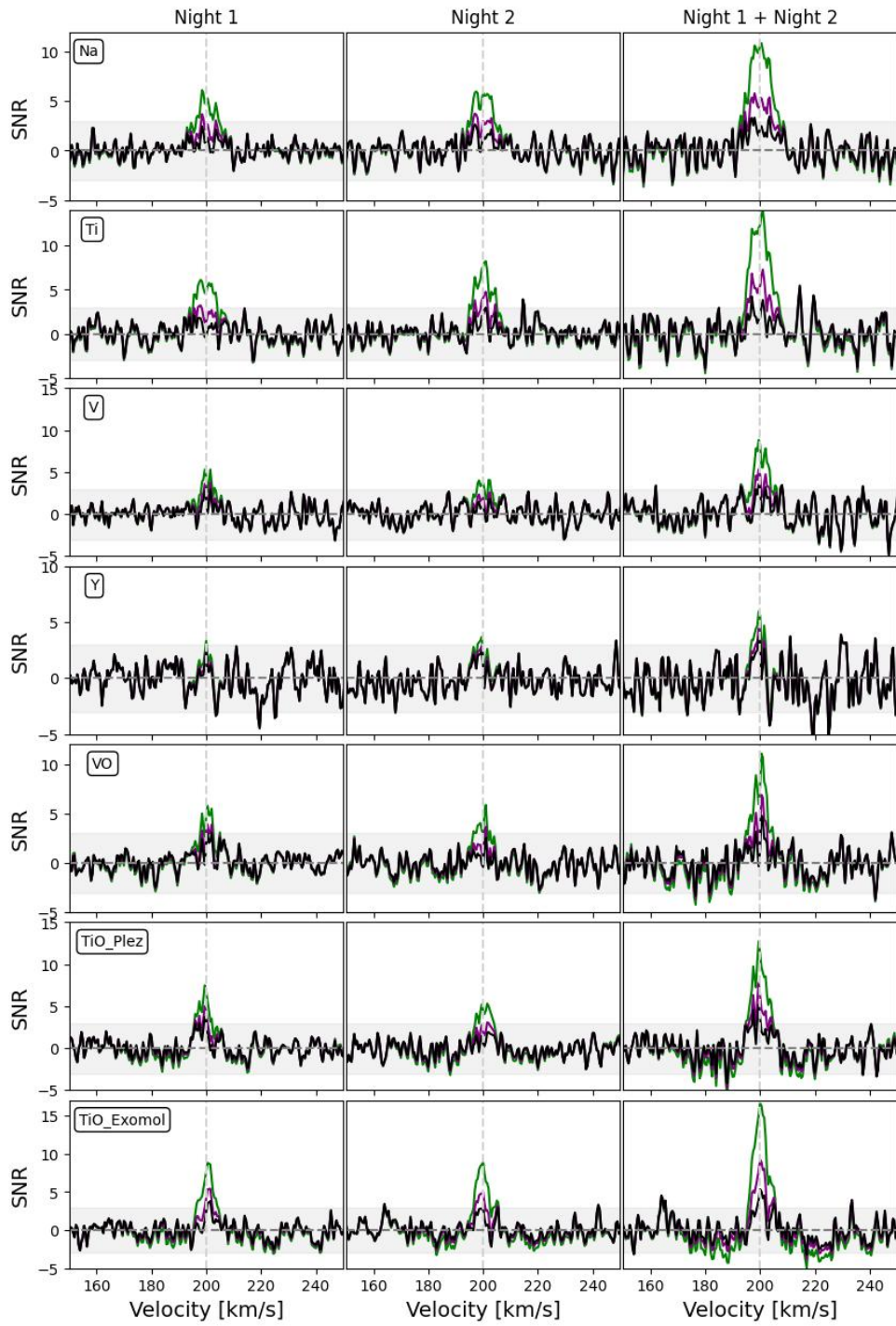


Fig. A.8: Same as Fig. A.7, but for Na I, Ti I, V I, Y I, VO, and TiO.

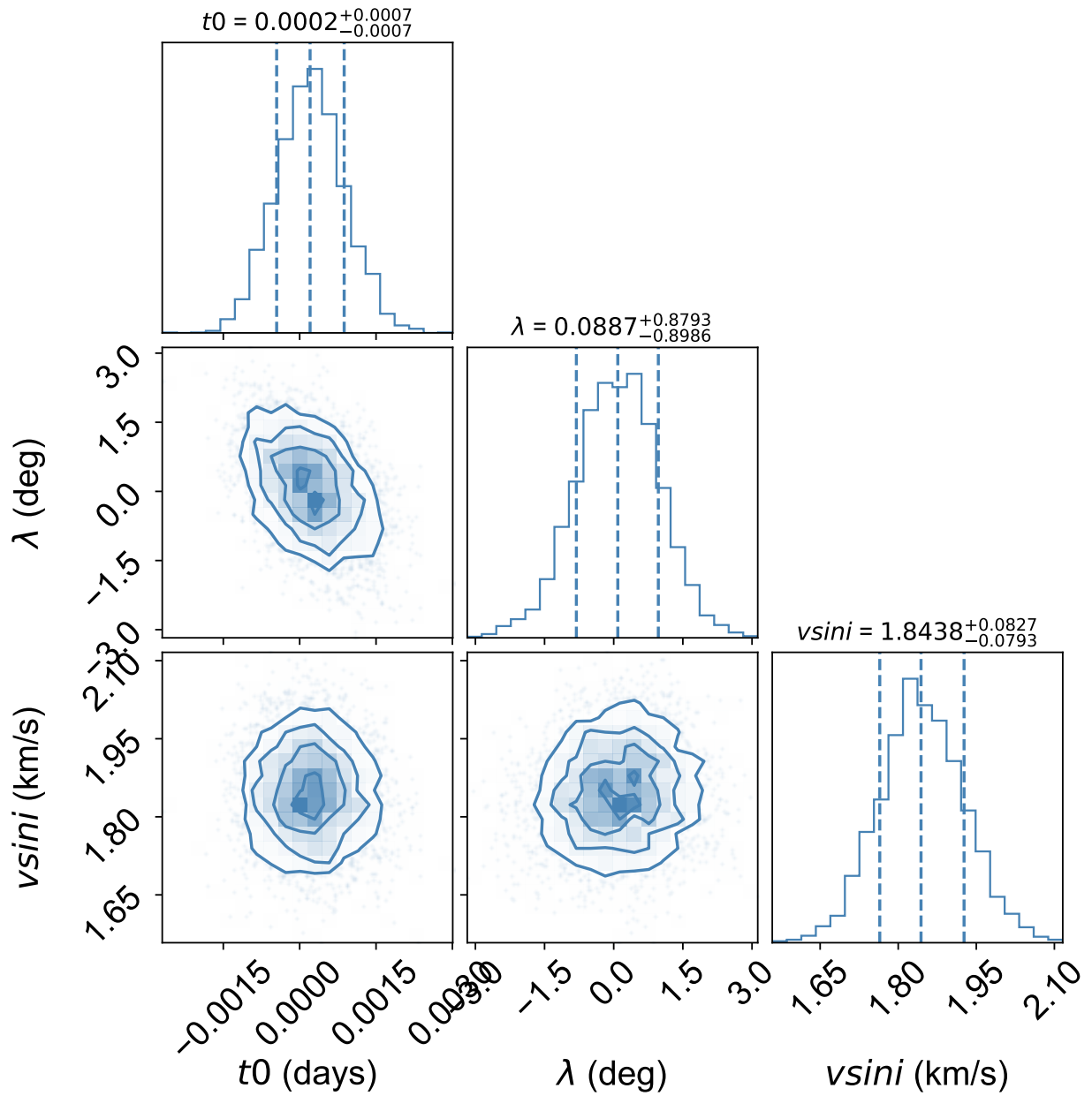


Fig. A.9: Corner plot resulting from the ARoME + emcee fitting. The mid-transit time (t_0), sky-projected spin-orbit angle (λ), and the projected stellar rotational velocity ($v \sin i$) parameters are left free during the fitting.